Improved chemical compatibility of zeolite and organic polymer for salt rejection and fouling resistance performance of the asymmetric hybrid polyamide-based reverse osmosis membrane

Nguyen Xuan Que Vo[1, 2], Tuan Van Doan[3], Nguyen Xuan Phuong Vo[4*]

[1]Faculty of Environment and Natural Resources, Ho Chi Minh City University of Technology, 268 Ly Thuong Kiet Street, District 10, Ho Chi Minh City, Vietnam
[2]Vietnam National University, Ho Chi Minh City, Linh Trung Ward, Thu Duc District, Ho Chi Minh City, Vietnam
[3]Eco Technology Vietnam Ltd., 225 Huynh Tan Phat Street, Phu My Ward, Phu My Township, Ba Ria - Vung Tau Province, Vietnam
[4]Faculty of Applied Sciences, Ton Duc Thang University, 19 Nguyen Huu Tho Street, Tan Phong Ward, District 7, Ho Chi Minh City, Vietnam

Received 21 June 2024; revised 30 July 2024; accepted 17 October 2024

Abstract:

An asymmetric configuration of the reverse osmosis (RO) membrane was synthesised, consisting of a dense citrate-capped Ag^0/LTA/PES layer (67.5±7.4 µm thick) sandwiched between a porous PES/PE substrate (26.7±4.8 µm thick) and a dense citrate-capped Ag^0/LTA/PA layer (ca. 21.8±6.2 µm thick), constructed onto a bottom non-woven polyester layer (84.3±13.1 µm thick). Membrane permeability, salt rejection, and antifouling performance were attributed to superior hydrophilicity and the ion-sieving channels of microporous Al-rich Na-LTA (linde type A) zeolite, enhanced by the presence of extra-framework antimicrobial Ag^0 species. Negatively charged citrate caps on the Ag^0/LTA surface improved both stability and compatibility of the dispersed zeolite phase in the bulky polymer matrix. Under harsh operational conditions, characterised by high transmembrane pressure and feed solution heavily contaminated with NaCl and micro-organisms, a less severe trade-off between water permeability and salt rejection was observed as the citrate-capped Ag^0/LTA load increased to 14%. After 30 days of exposure to the contaminated feed at a high transmembrane pressure of 140 psi, the RO membrane with 14 wt.% citrate-capped Ag^0/LTA, containing negligible incompatible voids, produced a significantly high water flux (ca. 15.0 $l.m^{-2}.h^{-1}$), demonstrated improved fouling resistance, and maintained Cl^- rejection at 71%.

Keywords: **high throughput separation, hybrid membrane, inorganic-organic compatibility, reverse osmosis, surface modification.**

Classification numbers: **2.2, 5.3**

1. Introduction

The demand for clean water in daily life is increasing as a consequence of climate change and population growth [1]. Freshwater bodies are becoming contaminated with various pollutants from multiple sources, placing increasing pressure on current treatment processes. The rise in waterborne diseases has heightened public awareness of the need for safe and reliable water supplies. The growing demand for domestic water treatment to provide safe drinking water has made RO membranes a profitable market for technology providers. Thin-film composite (TFC) RO membranes effectively remove a wide range of chemical compounds, whether dissolved or suspended, as well as biological contaminants (primarily bacteria) from water. Currently, polyamide-based thin-film composite (PA-TFC) membranes are the most prevalent type of RO membrane on the market [2].

The PA-TFC membrane is typically constructed with a supportive layer of tightly bonded non-woven polyester fabric, 120-150 µm thick. This is followed by a poly-ether-sulphone porous layer, approximately 50 µm thick, and a dense polyamide layer, 0.2-2 µm thick, which overlays the supportive layer [3]. To date, the PA-TFC membrane remains the best option for RO filtration applications, as it delivers greater osmotic flow at equal inlet pressure and stable resistance against microbiological organisms across a wide pH range [4]. However, the application of PA-TFC membranes is hindered by unresolved issues that limit their operational lifetime.

The primary obstacle to the application of PA-TFC membranes is the blockage of membrane surfaces and structural pores by micro-organisms, solutes, colloids, and cell debris, collectively known as external and internal fouling [5]. The consequences of fouling include decreased permeate flux, increased energy consumption, and reduced operational cost efficiency [6]. Biofilm formation on the polyamide surface layer enhances the adhesion of dissolved salts and organic matter, deteriorating the surface and reducing both productivity and permeate quality, while increasing operational costs [7]. Membrane fouling results in higher water pretreatment requirements, elevated pressure operations, frequent chemical cleaning, and eventual membrane replacement after 1-2 years, accounting for 24% of operational costs for full-scale RO systems [8].

*Corresponding author: Email: vonguyenxuanphuong@tdtu.edu.vn

Numerous studies have sought to mitigate fouling issues in existing RO membrane configurations. Strategies include the addition of hydrophilic additives or the substitution of more hydrophilic monomers during the interfacial polymerisation to provide a better wettability and rougher surface [9, 10], surface modification of membrane layers by co-polymer grafting or hydrophilic polymer coatings [11, 12], patterning wrinkled polymer surfaces for antifouling improvement [13, 14], and incorporating nanoparticles to solve the permeability-selectivity trade-off and to reduce fouling [15-19]. Among these solutions, the inorganic-organic hybrid membrane, in which nano-sized inorganic fillers are well dispersed in the entire polymer matrix, has attracted great attention due to improved membrane stability and separation performance. Specifically, nanoparticle-configured membranes have been exploited to their full extent to achieve advantages like efficiency and processability from the matrix of inorganic and polymer materials. It has been shown that inorganic fillers improve the compaction resistance of high-flux RO membranes [20]. Superior hydrophilicity, high negative surface charge, and internal pores of nano-sized inorganic fillers facilitate water absorption and movement across the membrane while maintaining high salt rejection [21]. Porous inorganic fillers such as zeolite and silica nanoparticles have inter-crystalline interconnections and tuneable pore sizes that are well below the size of hydrated salt ions (e.g., hydrated Na^+ 0.358 nm, hydrated Cl^- 0.332 nm) and at sizes greater than that of water (i.e., kinetic diameter of 0.275 nm) [22-24]. Hence, the porous structure of inorganic fillers provides not only a favourable path for water passing the membrane, but also a great selective blocking of dissolved organic substances and ion transports [16]. Apart from improved ion selectivity and huge specific surface areas, typical cation-exchange properties of zeolites make them ideal for carrying biocide agents. The simulation of zeolite molecular dynamics under a hydrostatic pressure and equilibrium condition demonstrated that the hybrid membrane comprising different loadings of porous nanoparticles can conduct water efficiently up to 5-1000 times the rate of commercially available TFC-RO membranes [25]. So far, zeolite and carbon nanotube (CNT) are most likely promising materials for performance enhancement of thin-film nano-composite RO membranes. Studies have shown the incorporation of different kinds of the inorganic fillers into the polymer matrix could be done using different approaches. S. Karki, et al. (2024) [26] employed spray coating and vapour-phase interfacial polymerisation to incorporate amine-functionalised graphene oxide into a thin-film nanocomposite membrane to significantly reduce reagent consumption and eliminate the need for organic solvent. D. Yadav, et al. (2024) [27] stated that the green and sustainable process of vapour-phase interfacial polymerisation on the surface of the polysulfone (PSf) support membrane between an aqueous phase solution of 3,5-diaminobenzoic acid (DABA) and vapours of trimesoyl chloride (TMC) also boosts the fabricated membranes' selectivity for pharmaceutical compounds [27]. However, considering the ease of processibility and scaling up, pre-mixing inorganic fillers with monomer solutions has been adopted in most works due to the process' simplification [28-31]. However, the dispersion of high loading of the nanoparticles into polymer layers would lead to agglomeration of the inorganic particles and defect formation at the polymer/inorganic particle interface due to increased chemical incompatibility between the two phases [32]. These defects have detrimental effects on the integrity and thus, the separation performance of membranes. Though many attempts to enhance the compatibility have been done by the surface modification of inorganic fillers [33, 34], it is questionable to which extent the surface modification of the inorganic fillers eliminates the interfacial defects between the inorganic and organic phases, and how positive compatibility effect correlates with the improved desalination and antimicrobial performance of the hybrid RO membrane.

In this work, LTA zeolite was chosen as the inorganic filler for membrane configuration because its pore sizes can be tuned from 0.23 to 0.42 nm [35], with the two extremes of this range being close to the sizes of water molecules and hydrated salt ions, respectively. Citrate-capped, Ag^0-embedded LTA zeolite was incorporated into the polymer layers of the RO membrane to enhance membrane hydrophilicity and introduce antimicrobial pathways for clean water production. Citrate ions were selected to act as both capping/reducing agents for Ag^+-exchanged LTA and crosslinking agents between Ag^0/LTA and polymer molecules. To facilitate the reduction of Ag^+, polyphenols from *Persicaria odorata* leaves were used, enabling the conversion of extra-framework Ag^+ in the LTA zeolite to Ag^0 via a green chemistry route. The extent of cross-linked density between the purely inorganic Ag^0/LTA and the purely organic poly-ether-sulfhone or polyamide polymer molecules, mediated by hydrogen bonding and coulombic forces, was hypothesised to determine the extent of detrimental defects in the resulting RO membranes.

This study aims to explore the effects of citrate-capped, Ag^0-embedded LTA zeolite on desalination and anti-biofouling performance by quantifying the number and size of confined spaces and voids within the hybrid membranes. From this, the chemical compatibility between the inorganic zeolite filler and the organic polymer matrix was correlated with overall membrane performance.

In this work, instead of varying the transmembrane pressure, the pressure was fixed at 140 psi - substantially higher than the optimal range for RO membranes. The feed water was heavily contaminated with high levels of salt and micro-organisms to create harsh operating conditions, under which RO membranes are particularly prone to fouling. These conditions were intentionally selected to highlight differences in fouling resistance among the studied RO membranes over a relatively short period. A separate test was conducted on commercial RO membranes under the same fixed transmembrane pressure of 140 psi to demonstrate the comparability of the fabricated membrane with commercial PA-based RO membranes in desalinating synthetic brackish water.

2. Methods and experiments

2.1. Synthesis of Al-rich Na-LTA zeolite

A template-free, Al-rich Na-LTA zeolite with theoretical Si/Al molar ratios of 1.0 (*ca.*) was prepared. Distilled water, sodium aluminate (Sigma-Aldrich®, Merck), sodium hydroxide (98%, Normapur®, Prolabo), and fumed silica (Sigma-Aldrich®, Merck) were added at a time into the baffled beaker under vigorous stirring for 4 h. Molar composition of the synthesis mixture for the Al-rich LTA zeolite was 1.0 Al_2O_3: 4.62 Na_2O: 2.14 SiO_2: 290 H_2O. The obtained gel was transferred to the Teflon-lined autoclave and aged for 15 h followed by a hydrothermal treatment at 373 K within 5 h. The powder was collected after cycles of centrifuging and washing in distilled water, followed by drying at 353 K for 24 h.

2.2. Synthesis of citrate-capped Ag^0-embedded linde type A inorganic filler

The Al-rich, Na-LTA zeolite powders were exchanged with 0.005 M $AgNO_3$ solution, with a solid-to-liquid weight-to-volume ratio of 2:100. The treatment was performed in a dark box, on a shaker, at room temperature for 24 h. The Ag^+-exchanged zeolite powders were obtained by centrifuging and washing in distilled water followed by drying at 353 K for 24 h. The obtained Ag^+-exchanged zeolite powders were dispersed in a polyphenol-rich extract solution from *Persicaria odorata* leaves (120.3 mg total polyphenols per 100 gr) to reduce the extra-framework Ag^+ cations to Ag^0 nanoparticles. Briefly, 1.0 g of the Ag^+-exchanged zeolite powders was dispersed into 100.0 ml of a dimethylformamide (DMF) (Sigma-Aldrich®, Merck) solution containing polyphenols (a reducing agent, total concentration of 120 mg/l) and tri-sodium citrate (a reducing agent and a stabiliser, final concentration of 5.0 mM). The mixture was stirred vigorously in a dark box at room temperature for 24 h. The citrate-capped Ag^0/Na-LTA powders were obtained after centrifuging and drying in vacuum at 333 K for 1 h. All samples were stored in a vacuum desiccator for further use.

2.3. Synthesis of thin film composite reverse osmosis membrane

Figure 1 illustrates a detailed experimental procedure for synthesising a thin film composite RO membrane. A solution of polyethersulfone (PES, Ultrason E6020P, MW=58,000 g/mol) in dimethylformamide (DMF, Merck) was prepared by slowly adding PES into a baffled bottle containing DMF at 343 K for 12 h under reflux with vigorous stirring. The non-woven polyester (PE) support was fixed on a heat-resistant glass plate (L x W x H = 20x10x5 cm) by a 3D tape. The solution of 21.5 wt.% PES in DMF was initially cast onto the PE support to form the PES/PE first layer. The citrate-capped Ag^0/LTA powders were dispersed slowly to the PES-DMF suspension for 3 h. Then the suspension of citrate-capp Ag^0/LTA in the PES-DMF solution was secondly cast onto the PES/PE first layer to form the

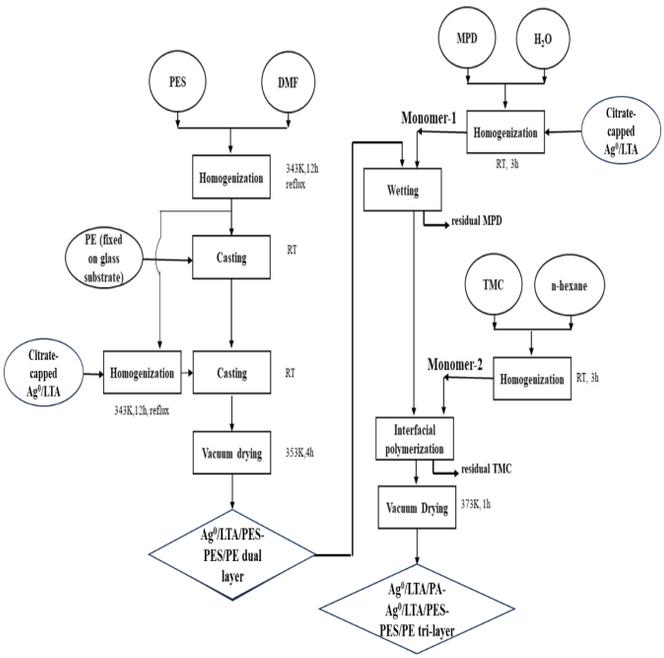

Fig. 1. Synthesis procedure for the thin film composite of an reverse osmosis membrane.

Ag^0/LTA/PES-PES/PE dual layer. Total loading of the citrate-capped Ag^0/LTA powders in the Ag^0/LTA/PES-PES/PE dual layer varied from 9,14, and 21 wt.%. The dual layer of hybrid materials was immersed in a water bath at room temperature for 24 h followed by vacuum drying at 353 K for 4 h.

For the synthesis of a thin polyamide layer on top of the dual layer, monomer solution #1 containing 1-methyl 2-pyrrolidinone (MPD) (Sigma-Aldrich®, Merck), water, and 1 wt.% citrate-capped Ag^0/LTA powders and solution #2 containing 1,3,5 benzene tricarbonyl trichloride (TMC) (Sigma-Aldrich®, Merck), and n-hexane (Sigma-Aldrich®, Merck) were separately prepared. The Ag^0/LTA/PES-PES/PE dual layer was fixed on the glass plate and the upper surface was wetted by solution #1. Excess solution #1 was removed from the upper surface before solution #2 was applied onto the wet layer of solution #1. The glass plate was put into vacuum oven and dried at 373 K for 1 h. The obtained asymmetric tri-layer was labelled as Ag^0/LTA/PA-Ag^0/LTA/PES-PES/PE.

2.4. Characterisation methods

Elemental contents of the samples were determined by inductively coupled plasma-mass spectrometry (ICP-MS) using a NexION®2000 (PerkinElmer, USA). Samples were digested in a 23-ml Teflon-lined stainless-steel acid digestion bomb (Parr Instruments) using a concentrated HNO_3: HF solution.

Nitrogen physisorption measurement at 77 K in TriStar 3020 Micromeritics unit was carried out to characterise the textural properties of the zeolite samples. Samples were degassed under

nitrogen flow at 673 K for 12 h prior to measurement. Surface areas and micropore volumes were calculated [36]. The Brunauer-Emmett-Teller (BET) method was used to calculate the total surface area. The t-plot method was used to estimate the micropore volume and the mesopore (external) surface area. Total pore volume and void volume fraction were computed following the protocol described in another study [37].

Crystalline structure of the samples was determined by X-ray powder diffraction (XRD) analysis. XRD patterns were recorded at room temperature from 2θ=5 to 80° with a step size of 0.026° on a Bruker D2 PHARSER diffractometer using Cu Kα radiation generated at 40 kV and 40 mA. Unit cell parameters were refined from the diffraction patterns using the Rietveld refinement function of the MATCH software package [38].

Hydrodynamic diameters of the citrate-capped Ag^0/LTA powders dispersed in the monomer solution #1 (Fig. 1) were determined by dynamic light scattering (DLS) technique using a SZ-100 Particle Analyzer (Horiba, Japan) at 298 K.

Morphology of zeolite samples and density of the deposited biofilm on the membrane surface were observed by scanning electronic microscopy (SEM/EDS). The images were taken over the Au-coated samples on a S-4800 FESEM (Hitachi, Japan) with a cold field-emission gun operating at 10 kV and 10 µA.

Thermogravimetric analysis and differential scanning calorimetry (LABSYS evo TGA/DSC 1600°C, Setaram Instrumentation) were used to investigate thermal stability and citrate content in the citrate-capped Ag^0/LTA powders. Measurements were carried out in nitrogen (99.99% purity, 10 ml/min) at a heating rate of 10 $K.min^{-1}$ from room temperature to 1173 K, with an initial sample weight of approximately 10 mg. Prior to measurements, the apparatus was calibrated according to the manufacturer's specifications in relation to weight, temperature and DSC calibrations.

The inorganic zeolite - polymer compatibility was evaluated via the measurement of available void space within the obtained Ag^0/LTA/PA-Ag^0/LTA/PES-PES/PE tri-layers with and without the citrate-capped Ag^0/LTA powders by positron annihilation lifetime spectroscopy (PALS). The PALS experiments were performed on identical 1-mm thick samples using a conventional fast-fast coincidence system at room temperature. A ^{22}Na radioactive source was covered by two thin aluminium foils and placed between the two identical membrane samples. The source correction was performed on the aluminium foils and two identical NaCl samples, and approximately 10% of positrons were found to be annihilated in the source. The membranes were degassed in-situ under vacuum condition at 373 K for 2 h. Each PALS spectrum had counts of about 3 million and a time resolution of about 220 ps full width at half-maximum (FWHM). The PALS spectra were best fitted by five or six exponential lifetime components corresponding to the annihilation of *para*-positronium *p*-Ps τ_1 <1 ns, direct annihilation of positron with free electrons τ_2 <1 ns, *ortho*-positronium *o*-Ps ($1<\tau_3<15$ ns; $1<\tau_4<15$ ns, $15<\tau_5<100$ ns and τ_6 >100 ns). The modified Tao-Eldrup (RTE) model was applied to estimate the equivalent pore diameter for a particular *o*-Ps lifetime based on the spherical pore geometry [39].

2.5. Performance evaluation of desalination and biofouling resistance of the Ag^0/LTA/PA-Ag^0/LTA/PES-PES/PE membrane

The desalination and biofouling-resistant performances of the hybrid Ag^0/LTA/PA-Ag^0/LTA/PES-PES/PE membrane and the pure organic PA-PES-PES/PE membrane were evaluated by a cross-flow RO water permeation apparatus in terms of water flux, percentage of NaCl salt removed from the feedwater stream, and density difference of biofilm deposited on the membrane surfaces. The apparatus consists of a home-made acrylic chamber with two rectangular windows on which a continuous groove with zig-zag pattern was mechanically engraved, as shown in Fig. 2. The cross-sectional dimensions of the grooves are approximately 1x1 mm. A layer of the synthesised membrane with an effective area of 25 cm^2 was assembled between the two opposite windows along with two square Teflon seals to create feed and permeate compartments.

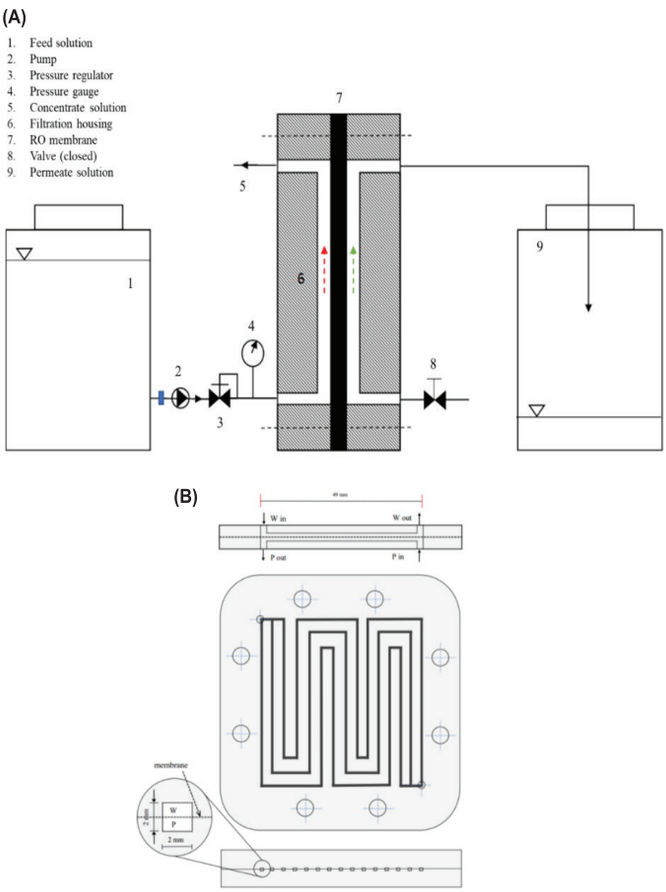

Fig. 2. (A) Sketch of lab-scale reverse osmosis system and (B) schematic of the filtration housing for permeability tests.

The synthetic solution of microbially-contaminated brackish water was used to estimate the salt rejection and anti-biofouling performance. NaCl and biogas sludge waste were mixed with water to prepare the contaminated feed containing 2000 mg/l NaCl, total coliforms of $15x10^3$ CFU/ml, total suspended solids (TSS) of 314.7 mg/l, and chemical oxygen demand (COD) of 178.3 mg/l. The pH of the simulated solution was 7.6±0.7. The transmembrane pressure was kept at 140 psi and the operating temperature was maintained at 298 K. The active side of the membranes was placed in contact with the contaminated feed solutions. After the membranes were compacted for 2 h to reach the steady state, the membrane performance was measured for 30 days. The water flux can be calculated by measuring the volume of the water penetrated through the membranes per effective volume per unit time ($L.m^{-3}.h^{-1}$) as follows:

$$J_v = \frac{Q_p}{S.l}$$

where S is the effective area of the membrane (m^2), l is the membrane thickness (m), and Q_p is the volumetric flow rate ($L.h^{-1}$).

The salt rejection (SR, %) can be calculated from Cl^- concentrations in the feed stream and permeance stream. The concentration of Cl^- was determined by the Mohr method of precipitation titration using 0.1 N $AgNO_3$ as a standard. After the performance test, the biofouling resistance can be visually determined by comparing the density of the biofilm deposited on the membranes with and without citrate-capped Ag^0/LTA, using SEM. In addition, the anti-fouling performance of the membrane was determined indirectly via a relative flux reduction of distilled water (RFR_{dw}, %), which is calculated as follows:

$$RFR_{dw} = \left(1 - \frac{J_{v1}}{J_{v0}}\right) x100\%$$

where J_{v1} and J_{v0} are the fluxes of distilled water permeated through the membrane after and before the 30-day exposure to the simulated solution contained NaCl and biogas sludge waste.

3. Results and discussion

3.1. Characterisation of the as-synthesised zeolite and the Ag^0-embedded zeolite sample

Figure 3 shows the XRD patterns of the as-synthesised LTA and Ag^0-embedded LTA samples. The XRD patterns of the as-synthesised LTA and Ag^0-embedded LTA samples matched the characteristic reflections of LTA structure [40]. For the LTA samples, the observed XRD patterns indicated that these samples exhibited cubic symmetry with space group of Pm-3m (No. 221). For the Ag^0-embedded LTA, the XRD patterns indicate that Ag nanoparticles were more likely to be well embedded in the LTA frameworks. The Ag^0-embedded LTA retained its crystal structure after the Ag^+ exchange and the reduction steps.

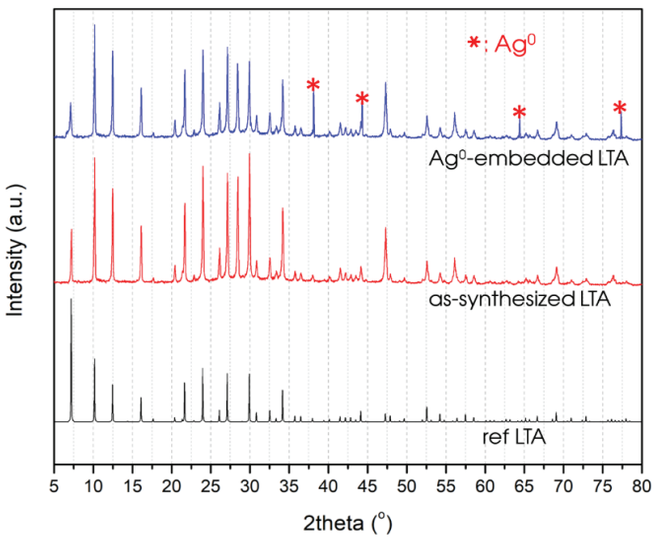

Fig. 3. X-ray powder diffraction patterns of the as-synthesised Na-LTA and Ag^0-embedded Na-LTA samples. The reflection pattern of linde type A zeolite from the International Zeolite Association Structure Commission is included as a reference [40].

As shown in the XRD pattern measured over the Ag^0-embedded LTA, the diffraction peaks decreased slightly in areas and intensities. This could be attributed to lattice distortion to some extent in the crystalline phases of the embedded LTA sample due to the exchange of the larger Ag^+ cations with smaller Na^+ cations within the zeolite frameworks. The refined unit cell parameters *a, b, c* and the unit cell volume *V* of the as-synthesised LTA and Ag^0/LTA structures are shown in Table 1. It can be seen that a contraction in unit cell volume of the LTA sample occurred during the exchange of Ag, specifically, a volume contraction of 3.69 $Å^3$ was detected in the Ag^0-embedded LTA unit cell.

Table 1. Unit cell dimensions *a, b, c* (Å) and unit cell volumes *V* ($Å^3$) of the as-synthesised Na-LTA and the Ag^0-embedded Na-LTA samples.

Samples	Unit cell parameters			
	a (Å)	*b* (Å)	*c* (Å)	*V* ($Å^3$)
Na-LTA	12.321(2)	12.321(2)	12.321(2)	1870.51
Ag^0/LTA	12.313(1)	12.313(1)	12.313(1)	1866.82

Molar compositions of the as-synthesised LTA and the Ag^0-embedded LTA samples were determined by the ICP-MS technique. The results are presented in Table 2. As shown in Table 2, practical value of Si/Al molar ratio of the as-synthesised LTA was 1.2. The value of Si/Al ratio in the Ag^0-embedded LTA sample appeared to be almost the same to the Si/Al ratio in the as-synthesised LTA. Thus, one can say that the framework Si and Al atoms in the LTA zeolite frameworks were not affected by the Ag^+ exchange procedure. The extents of exchanging Na^+ for Ag^+ in the embedded LTA was 33.7%. The calculated void volume fraction

of the as-synthesised LTA (Si/Al ratio of 1.2) sample obtained in this work is 48%. This remarkably open framework with high internal void space of the LTA sample would explain the ready accommodation of the significantly high amount of Ag^+ cations to its abundant Na^+ cation sites.

Table 2. Molar composition of the as-synthesised Na-LTA and the Ag^0-embedded Na-LTA samples.

Samples	Product composition		
	*Ag exchange degree (%)**	*Molar composition**	*Si/Al ratio**
Na-LTA	-	$Na_{13}Al_{13}Si_{11}O_{48}$	1.22
Ag^0/LTA	33.69	$Ag_{4.38}Na_{8.62}Al_{13}Si_{11}O_{48}$	1.20

*: Determined by inductively coupled plasma mass spectrometry.

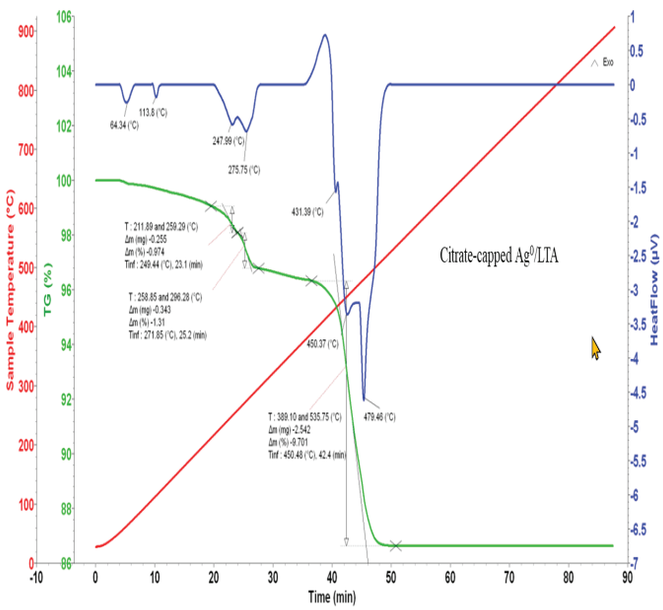

Fig. 4. Thermogravimetric analysis and differential scanning calorimetry curves of the citrate-capped Ag^0/LTA powders.

Figure 4 shows thermal effects and relevant mass losses that occurred when the citrate-capped Ag^0/LTA sample was heated in a nitrogen flow of 50 $ml.min^{-1}$ at a heating rate of 10 $K.min^{-1}$. The citrate-capped Ag^0/LTA sample displayed endothermic peaks within 337-387, 531-548, and 673-765 K, which are attributed to dehydration of physi sorbed water on the surface, de-hydroxylation of structural water and decomposition of the citrate caps, respectively. A weight loss of 9.96% was found in the temperature range of 673-765 K, referring to the amount of the citrate caps in the citrate-capped Ag^0/LTA.

The morphology of the as-synthesised LTA and Ag^0-embedded LTA particles are illustrated in Fig. 5. It can be seen from the SEM images in Fig. 5 that the as-synthesised LTA and Ag^0-embedded LTA particles have uniform cubic shape. For the embedded samples, the fact that no silver nanoclusters were found to deposit on the surfaces of the zeolites provides the proof that the silver nanoclusters were well embedded within the materials' framework.

The particle size distribution of the citrate-capped Ag^0/LTA powders dispersed in the MPD solution is also illustrated in Fig. 5. The measurement showed that the citrate-capped Ag^0/LTA powders have a narrow particle size distribution with a mean particle size of ca. 269 nm.

Figure 6 shows surface view and cross view of the as-synthesised, asymmetric Ag^0/LTA/PA-Ag^0/LTA/PES-PES/PE membrane. The SEM images reveal that the membrane surface has no open voids, pin holes, or cracks, which are good indicators of a dense, flawless membrane. The membrane cross view reveals the asymmetric configuration of the membrane, consisting of a

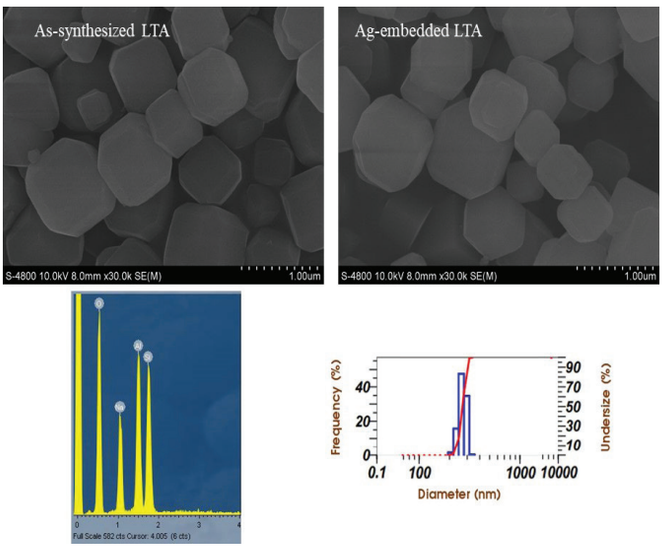

Fig. 5. Scanning electron microscopy combined with energy-dispersive X-ray spectroscopy analysis of the as-synthesised Na-LTA and Ag^0-embedded Na-LTA samples. Dynamic light scattering measurement of the citrate-capped Ag^0/LTA capsule dispersed in the m-phenylenediamine solution is also included.

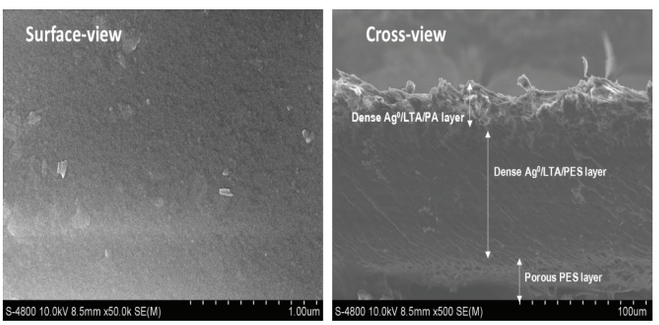

Fig. 6. Scanning electron microscopy image of surface view and cross view of the asymmetric Ag^0/LTA/PA-Ag^0/LTA/PES-PES/PE sample.

dense Ag^0/LTA/PES layer in sandwich between a porous PES/PE substrate and a dense Ag^0/LTA/PA layer. The perfect homogeneity of the Ag^0/LTA/PA top layer and the Ag^0/LTA/PES intermediate layer reveals that the polymers and the inorganic citrate-capped Ag^0/LTA filler are highly compatible during mixing. No bubbles or voids were observed in the boundary between the organic polymer matrix and the inorganic filler.

Table 3 illustrates BET specific surface areas and pore volumes of the as-synthesised Na-LTA and Ag^0-embedded Na-LTA, which were derived from the N_2 adsorption - desorption isotherms. The N_2 isotherms showed that all of the samples exhibit reversible type-I isotherm according to the IUPAC classification [38], which are given by the microporous solids having small external surfaces. This is in line with the dominant microporosity (e.g. micropores' surfaces and volumes) in all the samples shown in Table 3. It is evident from Table 3 that the BET surface area and the microporosity of the LTA decrease notably whereas the value of external surface area for the sample increases after the Ag^+ exchanged treatment. This can be explained by the fact that the Ag^+-exchanged treatment might cause an alteration in the zeolite frameworks in addition to the pore blocking effect due to the presence of Ag nanoclusters in the zeolite micropores. This also agrees well with the calculated unit cell contractions in the Ag^0-embedded LTA, as shown in Table 1.

Table 3. Textural properties of the as-synthesised Na-LTA and the Ag0-embedded Na-LTA samples.

Samples	Textural properties					
	S_{BET} $(m^2/g)^a$	S_{micro} $(m^2/g)^b$	S_{meso} $(m^2/g)^c$	V_{total} $(cm^3/g)^d$	V_{micro} $(cm^3/g)^e$	V_{meso} (cm^3/g)
Na-LTA	422.41	403.10	19.31	0.29	0.25	0.04
Ag^0/LTA	413.48	345.63	67.85	0.18	0.13	0.05

[a]: BET surface area; [b]: t-Plot micropore area; [c]: t-Plot external surface area; [d]: Single-point adsorption total pore volume of pores at p/p_o=0.97; [e]: t-Plot micropore volume.

3.2. Chemical compatibility between the citrate-capped Ag^0/LTA powders and the polymer matrix

The Ag^0/LTA/PES-PES/PE dual-layers with various loading of the citrate-capped Ag^0/LTA powders were made following the procedure shown in Fig. 1. Table 4 shows the PALS results of the pressed citrate-capped Ag^0/LTA pellets. Discrete values of lifetime and intensity derived from the PALS analysis of the Ag^0/LTA/PES-PES/PE dual-layers with various loadings of the citrate-capped Ag^0/LTA powders are shown in Table 5. For materials with 3D networks of corrugated pores, these lifetime components have been credited to *o*-Ps annihilating in micropores ($P_{S(micro)}$, 1-15 ns), mesopores ($P_{S(meso)}$, 15-100 ns) and in vacuum ($P_{S(vacuum)}$, >100 ns) [35, 39-42] . Intensity attributed to each *o*-Ps lifetime component was normalised by the total intensity of *o*-Ps measured and shown in Table 5. For the zeolite-polymer hybrid materials, the normalised $P_{S(micro)}$ is the key attribute of the fraction of *o*-Ps trapping and annihilating within intrinsic micropores of the zeolite, within network micropores of the polymer segments and within interstitial micropores of the polymer aggregates [42, 43]. Attribution of the normalised $P_{S(meso)}$ is derived in a similar fashion. For purely microporous materials, the sum of normalised $P_{S(meso)}$ and $P_{S(vacuum)}$ attributed to the fraction of *o*-Ps that is able to diffuse out of the microporous domain to intragranular spaces or vacuum, and that potentially correlates with the framework accessibility from external surface or the pore connectivity [44, 45]. As the size of the empty void spaces in the materials correlates with the lifetime (τ) of *o*-Ps whereas the contribution of the empty void spaces in the materials correlates with the normalised intensity of *o*-Ps, it can be seen from Table 4 that the as-synthesised LTA sample is primarily microporous structure. Low value of the normalised intensities of

Table 4. Contributions derived from positron annihilation lifetime spectroscopy measurements of the Na-LTA and citrate-capped Ag^0/LTA powders.

Components	$P_{S(micro)1}$ $(1<\tau_3<15$ ns)	$P_{S(micro)2}$ $(1<\tau_4<15$ ns)	$P_{S(meso)}$ $(15<\tau_5<100$ ns)	$P_{S(vacuum)}$ $(\tau_6>100$ ns)
Na-LTA	*Total o-Ps intensity is 30.4%*			
Lifetime (ns)	1.30	-	18.9	111
Intensity (%)	19.3	-	2.3	8.7
Normalised (%)	63.5	-	7.6	28.8
Citrate-capped Ag^0/LTA	*Total o-Ps intensity is 38.2(3)%*			
Lifetime (ns)	1.43	5.2	20.2	119
Intensity (%)	21.0	6.1	3.8	7.2
Normalised (%)	54.9	16.0	10.1	18.9

Table 5. Contributions derived from positron annihilation lifetime spectroscopy measurements of the PA-PES-PES/PE tri-layers without and with various loading of the citrate-capped Ag^0/LTA powders.

Components	$P_{S(micro)1}$ $(1<\tau_3<15$ ns)	$P_{S(micro)2}$ $(1<\tau_4<15$ ns)	$P_{S(meso)}$ $(15<\tau_5<100$ ns)	$P_{S(vacuum)}$ $(>100$ ns)
PA-PES-PES/PE - 0wt.% citrate-capped Ag^0/LTA	*Total o-Ps intensity is 8.7%*			
Lifetime (ns)	1.39	3.87	-	-
Intensity (%)	4.6	4.1	-	-
Normalised (%)	52.9	47.1	-	-
PA-PES-PES/PE - 9wt.% citrate-capped Ag^0/LTA	*Total o-Ps intensity is 31.3%*			
Lifetime (ns)	1.40	6.8	19.3	109
Intensity (%)	5.7	14.2	4.6	6.8
Normalised (%)	18.2	45.4	14.7	21.7
PA-PES-PES/PE - 14wt.% citrate-capped Ag^0/LTA	*Total o-Ps intensity is 36.2%*			
Lifetime (ns)	1.41	6.9	20.1	109
Intensity (%)	5.1	17.3	5.6	8.2
Normalised (%)	14.1	47.8	15.5	22.7
PA-PES-PES/PE - 21wt.% citrate-capped Ag^0/LTA	*Total o-Ps intensity is 38.2%*			
Lifetime (ns)	1.40	8.3	20.9	109
Intensity (%)	3.9	18.2	6.7	9.4
Normalised (%)	10.2	47.6	17.5	24.6

o-$P_{S(meso)}$ component in the LTA zeolite indicates small contribution of the inter- and intra-granular mesoporosity within the sample. Two micropore lifetime components were seen in the LTA zeolite at 1.24±0.02 and 4.91±0.01 ns, corresponding to the equivalent diameter of 0.46±0.01 and 1.04±0.01 nm, respectively. These values are in nice agreement with the sizes of the LTA principal building units, which are supercages of ca. 1.14 nm in diameter interconnected by 8-membered ring openings with ca. 0.41-nm aperture [40]. Thus, it can be said that the longer micropore lifetime component is possibly associated with the annihilation of *o*-Ps within the dehydrated supercages, while the shorter micropore lifetime component is associated with the annihilation of *o*-Ps at the 8-membered ring apertures. It was found that the sum of the normalised mesopore and vacuum lifetime components in the as-synthesised Na-LTA pellet was considerably high, indicating a high probability of *o*-Ps diffusion out from the microporous zeolite framework to intragranular spaces or vacuum, or a well-connected pore system. This result confirms the high void volume fractions and supports the high exchange degree of Ag^+ cations in the as-synthesised Na-LTA as calculated in Section 3.1.

The embedding of Ag^0 and capping of citrate to the LTA zeolite appeared to have a confining effect to the *o*-Ps as the sum of normalised intensity of the smaller *o*-Ps lifetime ($1<\tau<15$ ns) components significantly increases while that of the larger *o*-Ps lifetime (>15 ns) components decreases. It can be explained by the coupling effect of confining the *o*-Ps movement within the narrower micropore networks due to the incorporation of Ag^0 nanoparticles and blocking partially the *o*-Ps movement along the porous network towards the external surfaces due to the citrate caps. The increased lifetimes of $P_{S(micro)1}$ and $P_{S(micro)2}$ component in the citrate-capped Ag^0/LTA samples reveal the contribution of additional porous networks from the added citrate caps and the potential boundary defect at the Ag^0/LTA and the citrate interphase. The average lifetimes representative of the micropore networks within the citrate-capped Ag^0/LTA sample are 1.43 and 5.21 ns, corresponding to the equivalent pore size of 0.51 and 1.08 nm, respectively. The increase in the average microporous size in the citrate-capped Ag^0/LTA sample is more likely to come from the contribution of the microporous voids within the citrate segments and the microporous voids surrounding the citrate agglomerates. The additional porous voids in the citrate-capped Ag^0/LTA sample seem to localise mainly in the microporous domain. However, a slight increase of normalised intensity of $P_{S(meso)}$ component in the citrate-capped Ag^0/LTA sample indicates a small extent of pore expansion towards mesopore range. It is in good agreement with the BET results of the citrate-capped Ag^0/LTA sample, as shown in Table 3.

The results obtained from the PALS analysis of the hybrid membrane with and without the inorganic filler, as shown in Table 5, characterise decisive properties of the membranes in any separation application, including the sizes and concentrations of the free volume spaces within the membranes as well as the accessibility of these internal spaces to the membrane surfaces. Analysis of the PA-PES-PES/PE tri-layer without the citrate-capped Ag^0/LTA powder shows a majority of *o*-Ps annihilating within two distinct micro-sized volumes with the average lifetimes of 1.39 and 3.87 ns (equivalent to the network pores' diameter of 0.44 and 0.83 nm). A slightly higher value of the normalised intensity of $P_{S(micro)1}$ compared to that of $P_{S(micro)2}$ in the PA/PES/PE tri-layer reveals that the probability of *o*-Ps formation in the free volumes between the polymers' segments within each polymer aggregates appears to be slightly higher than that in the interstitial spaces surrounded by the polymer aggregates. However, the addition of various loadings of the citrate-capped Ag^0/LTA nanoparticles into the PA-PES-PES/PE tri-layer increases remarkably the probability of *o*-Ps formation in larger pore sizes, as shown in Table 5. The normalised intensity of the smaller *o*-Ps lifetime ($1<\tau<15$ ns) components significantly decreases while that of the larger *o*-Ps lifetime (>15 ns) components slightly increases with increasing loads of the citrate-capped Ag^0/LTA filler. Not only did the number of larger micropores gradually increase, but pore sizes also enlarged from 0.83 to 1.11 nm with increasing filler load. In other words, the addition of the citrate-capped Ag^0/LTA nanoparticles filled most of the smaller micropores in the polymer tri-layer and added a small portion of the larger micropores into the existing porous network. In the presence of the citrate-capped Ag^0/LTA filler, the majority of the *o*-Ps annihilating in the membranes still occurred within the micropore ranges. However, it seems that the higher amount of the citrate-capped Ag^0/LTA loads added to the polymer matrix, the considerably higher sizes and densities of free volumes in ranges of mesopores and macropores. This finding suggests a trade-off between the water flux and the selectivity of salt rejection from the membranes with contents of the citrate-capped Ag^0/LTA higher than 10 wt.% during the process of desalination.

3.3. Desalination and anti-biofouling performance

The Ag^0/LTA/PA-Ag^0/LTA/PES-PES/PE membranes with average thickness of 148±10 µm carrying various loads of Ag^0/LTA filler (0, 9, and 14 wt.%) were allowed to contact with the simulated solution in the filtration housing for 30 days for evaluation of desalination and anti-biofouling performance. The results of desalination performance of the membranes are shown in Fig. 7. The results clearly indicate the trade-off between permeability and rejection efficiency of the RO membranes, especially the membrane without the filler. With the RO membrane purely made from polymers, the salt rejection remained significantly but the permeance decreased to a great extent over days upon the harsh condition of operation (i.e. high transmembrane pressure, high load of contaminants). The trade-off between the permeance and the selectivity seems less severe in the produced membrane with higher contents of the filler. It shows that the membrane with 9 wt.% load of Ag^0/LTA filler achieved good salt rejection capacity, starting from 78% in the first day up to 92% in the 30th day. The water flux permeated through the membrane with 9 wt.% load of Ag^0/LTA filler decreased from 11.3 $l.m^{-2}.h^{-1}$ to 8.2 $l.m^{-2}.h^{-1}$. It could be explained by the fast build-up of a fouling layer on the film surface, leading to clogging of salt ions over time under

the application of constant pressure. In contrast, the membrane with 14 wt.% load of Ag^0/LTA filler achieved lower salt rejection capacity, starting from 62% in the first day up to 71% in the 30th day. However, water was permeated through the membrane with 14 wt.% load of Ag^0/LTA filler at a higher flux, and the permeance decreased slightly from 16 to 14.5 $L.m^{-2}.h^{-1}$. It could be explained by the presence of many larger pores in the membrane with higher load of Ag^0/LTA, as confirmed by the PALS analysis.

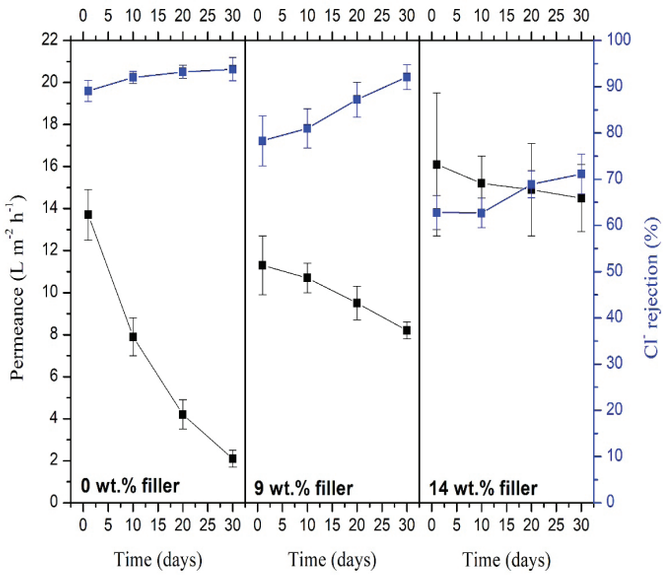

Fig. 7. Salt rejection capacity of the Ag^0/LTA/PA-Ag^0/LTA/PES-PES/PE membranes over time during the exposure to the contaminated feed solution.

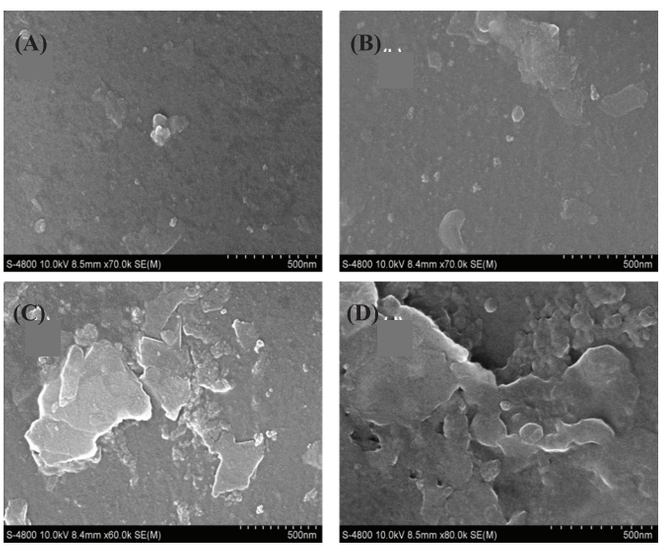

Fig. 8. Scanning electron microscopy images of surface of the as-synthesised Ag^0/LTA/PA-Ag^0/LTA/PES-PES/PE carrying 9 wt.% citrate-capped Ag^0/LTA filler. (A) After 1-day exposure; **(B)** After 10-day exposure; **(C)** After 20-day exposure; **(D)** After 30-day exposure.

Biomass of the fouling layer on surfaces of the Ag^0/LTA/PA-Ag^0/LTA/PES-PES/PE membranes with an average thickness of 148±10 µm carrying various loads of Ag^0/LTA filler (9 and 14 wt.%) was evaluated after the 30-day exposure. The density of the fouling layers was visualised by SEM images shown in Figs. 8 and 9 over different exposure periods. The anti-fouling resistance of the membranes was evaluated by the biomass accumulation onto the membranes' surfaces and the relative flux reduction of distilled water (RFR_{dw}) permeated through the tested membranes at the transmembrane pressure of 140 psi. SEM images in Figs. 8 and 9 clearly demonstrate the better resistance to fouling in the membrane with 14 wt.% Ag^0/LTA filler. The biomass of the deposited fouling layer on the membrane with 14 wt.% Ag^0/LTA filler was 12.5% after the 30-day exposure, which is much lower than 48.4% of fouling biomass on the membrane with 9 wt.% Ag^0/LTA filler. Similarly, RFR_{dw} of the membrane with 14 wt.% Ag^0/LTA filler was 41.4%, which is only half of RFR_{dw} of the membrane with 9 wt.% Ag^0/LTA filler (85.6%).

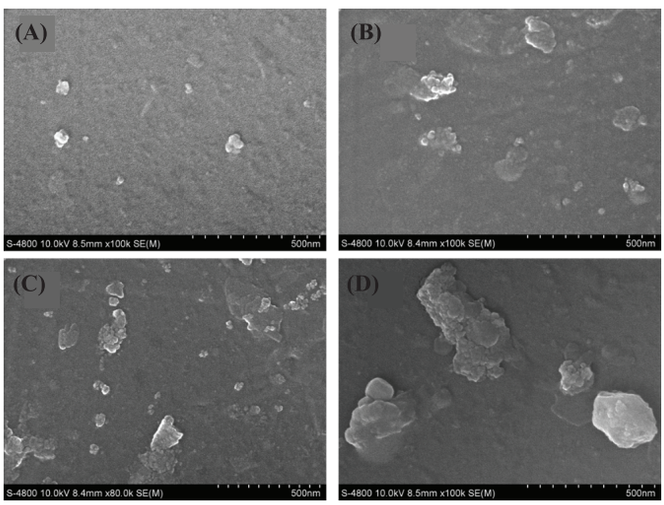

Fig. 9. Scanning electron microscopy images of surface of the as-synthesised Ag^0/LTA/PA-Ag^0/LTA/PES-PES/PE carrying 14 wt.% citrate-capped Ag^0/LTA filler. (A) After 1-day exposure; **(B)** After 10-day exposure; **(C)** After 20-day exposure; **(D)** After 30-day exposure.

Table 6. Comparison of desalination performance after 30-day exposure.

Membranes	Testing conditions	Performance (30-day exposure)	
		Permeance ($L.m^{-2}.h^{-1}$)	*Cl^- removal (%)*
BW30_PA-TFC_RO*	Synthetic solution: 2,000 mg/l NaCl; Coliforms of $15x10^3$ CFU/ml; TSS of 314.7 mg/l; pH=7.6±0.7; Applied pressure: 140 psi; Active membrane area: 25 cm^2; Temperature: 25°C	13.4±2.9	79.4±3.8
The studied membrane (14wt.% citrate-capped Ag^0/LTA)		16.3±4.2	71.3±5.1

*: Dow filmtec flat sheet membrane, original size of 305x305 mm, application of brackish water desalination.

An additional test of the performance of a commercial PA RO membrane (dow filmtec flat sheet membrane) in desalination of the synthetic brackish solution contaminated with micro-organisms was done after 30 days exposure. The desalination performance of the commercial membrane was compared to that of the membrane fabricated in this study with 14 wt.% citrate-capped Ag^0/LTA and the results were shown in Table 6. It has been observed that the studied membrane with 14 wt.% citrate-capped Ag^0/LTA enhanced the water permeance through the membrane, compared to the commercial one. The removal of Cl^- through the studied membrane was a little lower, but still remained in a comparable range compared to that of the commercial membrane.

4. Conclusions

This work demonstrates the correlation of sizes and densities of empty void spaces within the hybrid, asymmetric RO membrane carrying various loads of citrate-capped Ag^0/LTA nanoparticles and the membrane performance in desalination. The PALS results indicate that the porous networks within the citrate-capped Ag^0/LTA filler are mainly micropores with pore sizes of 0.51 nm and 1.08 nm, which were supposedly originated from the contribution of the partially-blocked micropores in Ag^0/LTA and the microporous voids within the citrate segments and surrounding the citrate agglomerates. PALS analysis of the purely organic membrane of PA-PES-PES/PE shows a majority of micro-sized volumes with the average diameters of roughly 0.44 and 0.83 nm, which came from both the free volumes between the polymers' segments within each polymer aggregates and the interstitial spaces surrounded by the polymer aggregates. However, the addition of various loadings of the citrate-capped Ag^0/LTA nanoparticles into the PA-PES-PES/PE tri-layer increases not only the number but also the size of larger micropores from 0.83 to 1.11 nm. It is reasonable to assume the addition of the citrate-capped Ag^0/LTA nanoparticles filled up most of the smaller micropores in the polymer tri-layer and added a small portion of the larger micropores into the existing porous network. Though the small contribution of larger pores in the mesopore and macropore ranges was found in the hybrid membrane carrying 14 wt.% filler, the internal fouling and external fouling of the membrane were improved to a great extent. The obtained hybrid membrane with 14 wt.% filler therefore exhibited a significantly high flux of water (ca. eight-fold as much as that produced from the pure polymer membrane), an improved biofouling resistance capacity, and thus a steady efficiency of salt rejection, as comparable to those of the commercial membrane for brackish water desalination.

CRediT author statement

Nguyen Xuan Que Vo: Data curation, Writing - Original draft preparation; Tuan Van Doan: Methodology, System development; Nguyen Xuan Phuong Vo: Conceptualisation, Visualisation, Supervision, Writing - Reviewing and Editing.

ACKNOWLEDGEMENTS

The authors acknowledge Korea Institute of Science and Technology (KIST) and Ho Chi Minh City University of Technology (HCMUT), VNU-HCM for supporting this study.

COMPETING INTERESTS

The authors declare that there is no conflict of interest regarding the publication of this article.

REFERENCES

[1] B.K. Arsiso, G.M. Tsidu, G.H. Stoffberg, et al. (2017), "Climate change and population growth impacts on surface water supply and demand of Addis Ababa, Ethiopia", *Climate Risk Management*, **18**, pp.21-33, DOI: 10.1016/j.crm.2017.08.004.

[2] A.L. Larranaga, J.L. Aguirre, J.S. Salinas, et al. (2022), "Thin film composite polyamide reverse osmosis membrane technology towards a circular economy", *Membranes*, **12(9)**, DOI: 10.3390/membranes12090864.

[3] F. Liu, L. Wang, D. Li, et al. (2019), "A review: The effect of the microporous support during interfacial polymerization on the morphology and performances of a thin film composite membrane for liquid purification", *RSC Advances*, **9**, pp.35417-35428, DOI: 10.1039/C9RA07114H.

[4] Z. Yang, Y. Zhou, Z. Feng, et al. (2019), "A review on reverse osmosis and nanofiltration membranes for water purification", *Polymers*, **11(8)**, DOI: 10.3390/polym11081252.

[5] M.A. Ahmed, S.Amin, A.A. Mohamed (2023), "Fouling in reverse osmosis membranes: Monitoring, characterization, mitigation strategies and future directions", *Heliyon*, **9(4)**, DOI: 10.1016/j.heliyon.2023.e14908.

[6] D. Yadav, S. Karki, P. G. Ingole (2022), "Current advances and opportunities in the development of nanofiltration (NF) membranes in the area of wastewater treatment, water desalination, biotechnological and pharmaceutical applications", *Journal of Environmental Chemical Engineering*, **10(4)**, DOI: 10.1016/j.jece.2022.108109.

[7] J.W. Koo, J.S. Ho, Y.Z. Tan, et al. (2021), "Fouling mitigation in reverse osmosis processes with 3D printed sinusoidal spacers", *Water Research*, **207**, DOI: 10.1016/j.watres.2021.117818.

[8] M. Jafari, M. Vanoppen, J.M.C. Agtmaal, et al. (2021), "Cost of fouling in full-scale reverse osmosis and nanofiltration installations in the Netherlands", *Desalination*, **500**, DOI: 10.1016/j.desal.2020.114865.

[9] G.R. Xu, J.N. Wang, C.J. Li (2013), "Strategies for improving the performance of the polyamide thin film composite (PA-TFC) reverse osmosis (RO) membranes: Surface modifications and nanoparticles incorporations", *Desalination*, **328**, pp.83-100, DOI: 10.1016/j.desal.2013.08.022.

[10] S. Yu, M. Liu, X. Liu, et al. (2009), "Performance enhancement in interfacially synthesized thin-film composite polyamide-urethane reverse osmosis membrane for seawater desalination", *Journal of Membrane Science*, **342(1-2)**, pp.313-320, DOI: 10.1016/j.memsci.2009.07.003.

[11] G.D. Kang, Z.N. Liu, H.J. Yu, et al. (2012), "Enhancing antifouling property of commercial polyamide reverse osmosis membrane by surface coating using a brush-like polymer containing poly (ethylene glycol) chains", *Desalination and Water Treatment*, **37(1-3)**, pp.139-145, DOI: 10.5004/dwt.2012.2783.

[12] L.P. Zhu, Y.Y. Xu, X.Z. Wei, et al. (2009), "Hydrophilic modification of poly(phthalazine ether sulfone ketone) ultrafiltration membranes by the surface immobilization of poly(ethylene glycol) acrylates", *Desalination*, **242(1-3)**, pp.96-109, DOI: 10.1016/j.desal.2008.03.034.

[13] H.S. Lim, S.Y. Lee, N.E. Lee, et al. (2018), "Patterning of wrinkled polymer surfaces by single-step electron irradiation", *Langmuir*, **34(18)**, pp.5290-5296, DOI: 10.1021/acs.langmuir.8b00403.

[14] D.H.K. Nguyen, V.T.H. Pham, V.K. Truong, et al. (2018), "Role of topological scale in the differential fouling of *Pseudomonas Aeruginosa* and *Staphylococcus Aureus bacterial* cells on wrinkled gold-coated polystyrene surfaces", *Nanoscale*, **10(11)**, pp.5089-5096, DOI: 10.1039/c7nr08178b.

[15] B.H. Jeong, E.M.V. Hoek, Y. Yan, et al. (2007), "Interfacial polymerization of thin film nanocomposites: A new concept for reverse osmosis membranes", *Journal of Membrane Science*, **294(1-2)**, pp.1-7, DOI: 10.1016/j.memsci.2007.02.025.

[16] M.T.M. Pendergast, J.M. Nygaard, A.K. Ghosh, et al. (2010), "Using nanocomposite materials technology to understand and control reverse osmosis membrane compaction", *Desalination*, **261(3)**, pp.255-263, DOI: 10.1016/j.desal.2010.06.008.

[17] V. Schwartz, F. Thetiot, S. Ritz, et al. (2012), "Antibacterial surface coatings from zinc oxide nanoparticles embedded in poly(n-isopropylacrylamide) hydrogel surface layers", *Advanced Functional Materials*, **22(11)**, pp.2376-2386, DOI: 10.1002/adfm.201102980.

[18] L. Li, J. Dong, T.M. Nenoff (2007), "Transport of water and alkali metal ions through MFI zeolite membranes during reverse osmosis", *Separation and Purification Technology*, **53(1)**, pp.42-48, DOI: 10.1016/j.seppur.2006.06.012.

[19] P. Lalueza, M. Monzon, M. Arruebo, et al. (2011), "Antibacterial action of Ag-containing MFI zeolite at low Ag loadings", *Chemical Communications*, **47(2)**, pp.680-682, DOI: 10.1039/c0cc03905e.

[20] I. Goossens, A.V. Haute (1976), "The influence of mineral fillers on the membrane properties of high flux asymmetric cellulose acetate reverse osmosis membranes", *Desalination*, **18(2)**, pp.203-214, DOI: 10.1016/S0011-9164(00)84102-8.

[21] A.A. Mayyahi (2018), "Important approaches to enhance reverse osmosis (RO) thin film composite (TFC) membranes performance", *Membranes*, **8(3)**, DOI: 10.3390/membranes8030068.

[22] A.G. Volkov, S. Paula, D.W. Deamer (1997), "Two mechanisms of permeation of small neutral molecules and hydrated ions across phospholipid bilayers", *Bioelectrochemistry and Bioenergetics*, **42(2)**, pp.153-160, DOI: 10.1016/S0302-4598(96)05097-0.

[23] E.R. Nightingale (1959), "Phenomenological theory of ion solvation. Effective radii of hydrated ions", *The Journal of Physical Chemistry*, **63(9)**, pp.1381-1387, DOI: 10.1021/j150579a011.

[24] P. Demontis, J.G. Gonzalez, H. Jobic, et al. (2008), "Dynamical properties of confined water nanoclusters: Simulation study of hydrated zeolite NaA: Structural and vibrational properties", *ACS Nano*, **2(8)**, pp.1603-1614, DOI: 10.1021/nn800303r.

[25] B. Corry (2008), "Designing carbon nanotube membranes for efficient water desalination", *The Journal of Physical Chemistry B*, **112(5)**, pp.1427-1434, DOI: 10.1021/jp709845u.

[26] S. Karki, P.G. Ingole (2024), "Spray coating vapor-phase interfacial polymerization: A new approach for developing 2D nanosheet enabled thin film nanocomposite membranes to remove heavy metal ions", *Chemical Engineering Journal*, **488**, DOI: 10.1016/j.cej.2024.150883.

[27] D. Yadav, M.B. Gohain, M. Bora, et al. (2024), "Greener synthesis of thin-film nanocomposite membranes with varied nanofillers for enhanced organic micropollutant removal", *Separation and Purification Technology*, **335**, DOI: 10.1016/j.seppur.2023.126125.

[28] H.R. Chae, J. Lee, C.H. Lee, et al. (2015), "Graphene oxide-embedded thin-film composite reverse osmosis membrane with high flux, anti-biofouling, and chlorine resistance", *Journal of Membrane Science*, **483**, pp.128-135, DOI: 10.1016/j.memsci.2015.02.045.

[29] H. Dong, L. Wu, L. Zhang, et al. (2015), "Clay nanosheets as charged filler materials for high-performance and fouling-resistant thin film nanocomposite membranes", *Journal of Membrane Science*, **494**, pp.92-103, DOI: 10.1016/j.memsci.2015.07.049.

[30] Q. Zhao, D.L. Zhao, T.S. Chung (2021), "Thin-film nanocomposite membranes incorporated with defective ZIF-8 nanoparticles for brackish water and seawater desalination", *Journal of Membrane Science*, **625**, DOI: 10.1016/j.memsci.2021.119158.

[31] M.A. Aroon, A.F. Ismail, T. Matsuura, et al. (2010), "Performance studies of mixed matrix membranes for gas separation: A review", *Separation and Purification Technology*, **75**, pp.229-242, DOI: 10.1016/J.SEPPUR.2010.08.023.

[32] H. Dong, X.Y. Qu, L. Zhang, et al. (2011), "Preparation and characterization of surface-modified zeolite-polyamide thin film nanocomposite membranes for desalination", *Desalination and Water Treatment*, **34(1-3)**, pp.6-12, DOI: 10.5004/dwt.2011.2789.

[33] Q. Fang, X. Liu, N. Wang, et al. (2015), "The effect of zeolite particle modified by PEG on rubber composite properties", *Science and Engineering of Composite Materials*, **22(6)**, pp.607-612, DOI: 10.1515/secm-2013-0316.

[34] T.M. Salama, I.O. Ali, A.I. Hanafy, et al. (2009), "A novel synthesis of NaA zeolite encapsulated iron(III) schiff base complex: Photocatalytic oxidation of direct blue-1 dye with hydrogen peroxide", *Materials Chemistry and Physics*, **113(1)**, pp.159-165, DOI: 10.1016/j.matchemphys.2008.06.075.

[35] American Society for Testing and Materials (2019), *D4365-19. Standard Test Method for Determining Micropore Volume and Zeolite Area of a Catalyst*.

[36] D. Ongari, P.G. Boyd, S. Barthel, et al. (2017), "Accurate characterization of the pore volume in microporous crystalline materials", *Langmuir*, **33**, pp.14529-14538, DOI: 10.1021/acs.langmuir.7b01682.

[37] K. Brandenburg, H. Putz (2020), "Match! - phase analysis using powder diffraction", https://www.crystalimpact.com/match/Default.htm:Crystal Impact, accessed 18 October 2023.

[38] T.L. Dull, W.E. Frieze, D.W. Gidley, et al. (2001), "Determination of pore size in mesoporous thin films from the annihilation lifetime of positronium", *The Journal of Physical Chemistry B*, **105(20)**, pp.4657-4662, DOI: 10.1021/jp004182v.

[39] International Zeolite Association (2022), *Database of Zeolite Structures*, https://www.iza-structure.org/databases/, accessed 18 October 2023.

[40] S. Grazulis, A. Daskevic, A. Merkys, et al. (2012), "Crystallography open database (COD): An open-access collection of crystal structures and platform for world-wide collaboration", *Nucleic Acids Res.*, **40(D1)**, pp.D420-D427, DOI: 10.1093/nar/gkr900.

[41] M. Thommes, K. Kaneko, A.V. Neimark, et al. (2015), "Physisorption of gases, with special reference to the evaluation of surface area and pore size distribution (IUPAC technical report)", *Pure and Applied Chemistry*, **87**, pp.1051-1069, DOI: 10.1515/PAC-2014-1117.

[42] Y. Kobayashi, K. Ito, T. Oka, et al. (2007), "Positronium chemistry in porous materials", *Radiation Physics and Chemistry*, **76(2)**, pp.224-230, DOI: 10.1016/j.radphyschem.2006.03.042.

[43] A. Zubiaga, R. Warringham, M. Boltz, et al. (2016), "The assessment of pore connectivity in hierarchical zeolites using positron annihilation lifetime spectroscopy: Instrumental and morphological aspects", *Physical Chemistry Chemical Physics*, **18(13)**, pp.9211-9219, DOI: 10.1039/c6cp00408c.

[44] R. Warringham, L. Gerchow, A. Zubiaga, et al. (2016), "Insights into the mechanism of zeolite detemplation by positron annihilation lifetime spectroscopy", *The Journal of Physical Chemistry C*, **120(44)**, pp.25451-25461, DOI: 10.1021/acs.jpcc.6b08931.

[45] M.S. Mauter, Y. Wang, K.C. Okemgbo, et al. (2011), "Antifouling ultrafiltration membranes via post-fabrication grafting of biocidal nanomaterials", *ACS Applied Materials & Interfaces*, **3(8)**, pp.2861-2868, DOI: 10.1021/am200522v.